



The influence of respiration on brainstem and cardiovagal response to auricular vagus nerve stimulation: A multimodal ultrahigh-field (7T) fMRI study

Roberta Sclocco ^{a, b, *}, Ronald G. Garcia ^{a, c}, Norman W. Kettner ^b, Kylie Isenburg ^a, Harrison P. Fisher ^a, Catherine S. Hubbard ^a, Ilknur Ay ^a, Jonathan R. Polimeni ^a, Jill Goldstein ^{a, c, d}, Nikos Makris ^{a, c}, Nicola Toschi ^{a, e}, Riccardo Barbieri ^{f, g}, Vitaly Napadow ^{a, b}

^a Athinoula A. Martinos Center for Biomedical Imaging, Department of Radiology, Massachusetts General Hospital, Harvard Medical School, Charlestown, MA, USA

^b Department of Radiology, Logan University, Chesterfield, MO, USA

^c Department of Psychiatry, Massachusetts General Hospital, Harvard Medical School, Boston, MA, USA

^d Department of Obstetrics and Gynecology, Massachusetts General Hospital, Harvard Medical School, Boston, MA, USA

^e Department of Biomedicine and Prevention, University of Rome Tor Vergata, Rome, Italy

^f Department of Electronics, Information and Bioengineering, Politecnico di Milano, Italy

^g Department of Anesthesia, Critical Care and Pain Medicine, Massachusetts General Hospital, Harvard Medical School, Boston, MA, USA

ARTICLE INFO

Article history:

Received 12 September 2018

Received in revised form

2 January 2019

Accepted 6 February 2019

Available online 10 February 2019

ABSTRACT

Background: Brainstem-focused mechanisms supporting transcutaneous auricular VNS (taVNS) effects are not well understood, particularly in humans. We employed ultrahigh field (7T) fMRI and evaluated the influence of respiratory phase for optimal targeting, applying our respiratory-gated auricular vagal afferent nerve stimulation (RAVANS) technique.

Hypothesis: We proposed that targeting of nucleus tractus solitarius (NTS) and cardiovagal modulation in response to taVNS stimuli would be enhanced when stimulation is delivered during a more receptive state, i.e. exhalation.

Methods: Brainstem fMRI response to auricular taVNS (cymba conchae) was assessed for stimulation delivered during exhalation (eRAVANS) or inhalation (iRAVANS), while exhalation-gated stimulation over the greater auricular nerve (GANctrl, i.e. earlobe) was included as control. Furthermore, we evaluated cardiovagal response to stimulation by calculating instantaneous HF-HRV from cardiac data recorded during fMRI.

Results: Our findings demonstrated that eRAVANS evoked fMRI signal increase in ipsilateral pontomedullary junction in a cluster including purported NTS. Brainstem response to GANctrl localized a partially-overlapping cluster, more ventrolateral, consistent with spinal trigeminal nucleus. A region-of-interest analysis also found eRAVANS activation in monoaminergic source nuclei including locus coeruleus (LC, noradrenergic) and both dorsal and median raphe (serotonergic) nuclei. Response to eRAVANS was significantly greater than iRAVANS for all nuclei, and greater than GANctrl in LC and raphe nuclei. Furthermore, eRAVANS, but not iRAVANS, enhanced cardiovagal modulation, confirming enhanced eRAVANS response on both central and peripheral neurophysiological levels.

Conclusion: 7T fMRI localized brainstem response to taVNS, linked such response with autonomic outflow, and demonstrated that taVNS applied during exhalation enhanced NTS targeting.

© 2019 Elsevier Inc. All rights reserved.

Introduction

The vagus nerve is critically involved in autonomic regulation of several visceral organs, including the heart, lungs, pancreas, and

* Corresponding author. Athinoula A. Martinos Center for Biomedical Imaging, Department of Radiology, Massachusetts General Hospital, Harvard Medical School, 149 13th St, Charlestown, MA, 02129, USA.

E-mail address: roberta@nmr.mgh.harvard.edu (R. Sclocco).

portions of the gastrointestinal tract. In the last couple of decades, the cervical bundle of the vagus (Cranial Nerve X) has been a target for vagus nerve stimulation (VNS) therapy. However, given the invasiveness and cost of the surgical VNS procedure, its therapeutic application has been mostly limited to brain-based targets: drug-resistant epilepsy and major depression [1–4]. More recently, two main non-invasive approaches (nVNS) have emerged, one targeting the cervical vagus nerve in the neck (transcutaneous cervical VNS, tcVNS), the other targeting the auricular branch of the vagus nerve (ABVN; transcutaneous auricular VNS, taVNS). The latter, taVNS, has been employed for patients suffering from various disorders including epilepsy [5], chronic tinnitus [6,7], depression [8,9], pain [10–13], migraine [12,14], as well as in cardiovascular modulation [15–17]. While clinical taVNS applications have been widely noted in the literature, the physiological mechanisms supporting such clinical effects are not well understood, particularly in humans.

The primary synaptic target of afference over the vagus nerve is the nucleus tractus solitarius (NTS), located in the dorsal medulla. This elongated nucleus extends rostroventrally from the pontomedullary junction to just below the obex, where it merges with the contralateral column. The NTS transfers information to premotor parasympathetic nuclei including nucleus ambiguus (NAmb) and dorsal motor nucleus of the vagus. In fact, taVNS has also demonstrated robust modulation of autonomic outflow using heart rate variability (HRV) and other measures [15,16,18]. Moreover, ascending projections from NTS transfer afference to higher monoamine neurotransmitter source nuclei such as locus coeruleus (LC, noradrenergic) and raphe (serotonergic) nuclei in the pons and midbrain [19–22], which may also impact autonomic outflow via feedback loops, as well as modulating higher brain function by recruiting these diffusely projecting neurotransmitter systems.

Importantly, NTS activity is known to be modulated by respiration, both through bottom-up afference from pulmonary stretch receptors and aortic baroreceptors, and via top-down influence from ventral respiratory group nuclei in the medulla. Specifically, NTS receives inhibitory influence during inhalation, and facilitatory influence during exhalation [23–25]. Therefore, our group has proposed that NTS targeting by taVNS can be enhanced by gating stimulation to the exhalation phase of the respiratory cycle via respiration-gated auricular vagal afferent nerve stimulation (RAVANS) [10,12]. In this context, exhalation-gated RAVANS (eRAVANS) produced promising antinociceptive effects compared to non-vagal auricular stimulation in chronic pain patients [10], and modulated trigeminosensory brain response in LC and raphe nuclei in migraine patients [12]. Thus, targeting NTS might be optimized by delivering stimulation during a more receptive state (i.e. exhalation).

Our study investigated evoked brain response to taVNS stimuli, which may support the neurophysiological and clinical effects noted above. While multiple functional magnetic resonance imaging (fMRI) studies have aimed at evaluating brain response to taVNS in humans [12,26–32], the challenges posed to brainstem functional imaging by physiological noise and the small cross-sectional area of many brainstem nuclei has limited signal-to-noise ratio (SNR) in such nuclei and hampered precise characterization of taVNS-related responses. Advances in ultrahigh-field MRI (UHF, 7T and higher) have proven instrumental in overcoming some of these SNR limitations, significantly expanding the field of brainstem imaging [33]. Our UHF fMRI approach sought to better localize evoked brainstem response to taVNS using focused cardiovascular noise removal and flexible hemodynamic response function setting, allowing us to reliably assess the influence of respiration-gating. Additionally, we evaluated concurrent instantaneous HRV response to taVNS using a statistical model-based spectral approach previously developed by our group [34] to investigate cardiovascular stimulus-evoked response, and tested the

association of the autonomic outflow with brainstem fMRI response. To our knowledge, this is the first study applying UHF fMRI to identify specific brainstem region responses to taVNS and link the response with autonomic outflow.

Methods

Subjects

Sixteen (16) healthy adult subjects (9 female, age: 27.0 ± 6.6 years, mean \pm SD) were enrolled. All study procedures were approved by the local Institutional Review Board, and written informed consent was provided by all subjects. Subjects were excluded from participation in case of major neurological or other medical disorders that would interfere with study procedures or confound results (e.g. conditions altering blood flow), a history of seizure or significant head trauma, a history of Axis I psychiatric diagnosis, as well as any contraindication for MRI. Prior to the MRI scanning, participants were familiarized with the stimulation and calibration procedure. Specifically, they were instructed to rate the intensity of the stimulation using a numeric rating scale (NRS) ranging from 0 (“no sensation”) to 10 (“pain threshold”), and to aim for a “moderately strong, but not painful sensation”, corresponding to a target score of 4–5 on the 0–10 scale. Subjects were told they would experience the stimulation intermittently during the imaging session. Subjects were not told, and were unaware of (by qualitative debriefing following the MRI scan session), respiration gating for any stimulation procedure during this study.

Experimental protocol

Each subject underwent a single visit MRI scan session consisting of four 8-min duration fMRI scan runs, including a passive control scan, two active stimulation scans, and an active control scan run (Fig. 1). Specifically, after an initial fMRI scan run during which sham stimulation was provided (i.e., electrode placed within cymba conchae, but no electrical current passed), subjects experienced three stimulation runs. For these scan runs, taVNS stimulation was gated either to the exhalation or inhalation phase of the respiratory cycle (eRAVANS, iRAVANS), while a third fMRI run included a control with exhalation-gated stimulation of the greater auricular nerve innervated earlobe location (GANctrl). The sham stimulation fMRI run was performed first in order to maintain blinding for active versus inactive stimulation, and the order of the three active stimulation runs was counterbalanced across subjects. Stimulus intensity (current amplitude, mA) was set by percept-matching across subjects (target score of 4–5 on the 0–10 NRS reported above) just prior to each scan run, and intensity ratings were assessed again at the end of each run.

Stimulation

Stimuli consisted of biphasic rectangular pulse trains with 450 μ s pulse width and a duration of 1 s, delivered at 25 Hz, and provided by a current-constant Model S88x stimulator with stimulus isolation unit (Grass Instruments, Astro-Med, Inc, West Warwick, RI, USA). RAVANS taVNS was delivered via custom-built, ergonomically-shaped MR-compatible electrodes (Bionik Medical Devices, Bucaramanga, Colombia) placed within the left cymba conchae of the ear (Fig. 1). A second set of electrodes was secured to the left earlobe prior to scanning, and used to deliver control-location stimulation (GANctrl). The respiratory gating was implemented by measuring respiration through a custom-built pneumatic belt placed around the subjects' lower thorax. Low-compliance tubing connected the belt to a pressure transducer

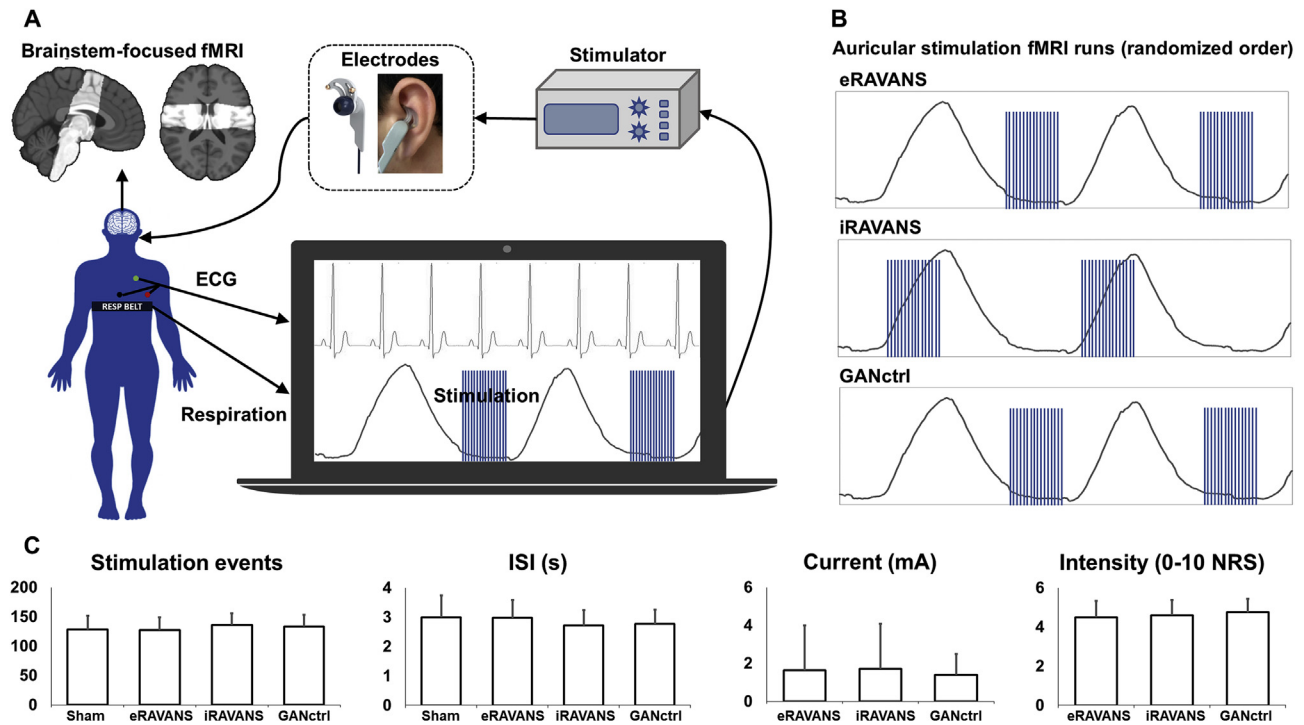


Fig. 1. (A) Experimental setup for data collection: fMRI data were collected with partial brain coverage focused on the brainstem (group-consistent coverage shown). Concurrently to fMRI, electrocardiography (ECG) and respiration signals were monitored, and the latter was used to trigger in real-time the onset of respiration-gated left auricular stimulation, delivered through custom electrodes placed either in the cymba conchae (RAVANS taVNS runs) or over the earlobe (greater auricular nerve control, GANctrl). (B) Example respiratory traces showing timing for exhalation-gated RAVANS (eRAVANS), inhalation-gated RAVANS (iRAVANS), and exhalation-gated GANctrl stimulation, counterbalanced across subjects. (C) Stimulation parameters (number of events, inter-stimulus interval (ISI), current) and ratings were not significantly different across conditions. Error bars represent SD.

(PX138-0.3D5V, Omegadyne, Inc., Sunbury, OH, USA), and the voltage signal reflecting respiratory volume was acquired by a laptop-controlled device (National Instruments USB DAQCard 6009, 14-bit i/o, with LabView 7.0 data acquisition software). In-house developed LabView® code was used to detect end-inhalation and end-exhalation in real-time, based on an adaptive threshold detection algorithm, and a TTL signal was sent to a miniature high-frequency relay (G6Z-1P-DC5, Omron Electronics Components, Schaumburg, IL, USA), thereby controlling the onset and offset of stimulation. **A brief 0.8 s delay was introduced between the end-inhalation timestamp and stimulus onset for exhalation-gated stimulation, in order to ensure delivery during the exhalation phase. As the inhalation phase is shorter than the exhalation phase, a nominal 0.1 s delay was used for inhalation-gated stimulation.** Potential differences in stimulation parameters and ratings across conditions were explored using repeated measures ANOVAs implemented in Matlab (R2016b, The MathWorks, Natick, MA, USA). Sham taVNS stimulation was provided during a separate fMRI scan run by disconnecting the stimulation electrode from the current source, while maintaining the identical auricular electrode placement on the subject.

MRI and physiological data collection

Blood oxygenation level-dependent (BOLD) fMRI data were collected on a Siemens 7 T whole-body scanner (Siemens Healthineers, Erlangen, Germany) using a custom-built 32-channel receive array and birdcage transmit coil. Functional MRI data were acquired with gradient-echo single-shot echo-planar imaging (EPI) using a Simultaneous Multi-Slice acquisition with multi-band factor 2 and the following parameters: 1.2 mm isotropic voxel size (field of view = $192 \times 192 \text{ mm}^2$), 38 coronal slices centered on the

brainstem and tilted parallel to the dorsal border of the brainstem using a mid-sagittal parallelizer, repetition time (TR) = 0.99 s, echo time (TE) = 23 ms, flip angle = 58° , band width = 1562 Hz pix^{-1} , echo spacing = 0.76 ms, using R = 4 in-plane (generalized autocalibrating partially parallel acquisitions (GRAPPA)) acceleration and a robust autocalibration scan [35]. For each fMRI scan run, 500 time-series measurements were acquired. To aid co-registration, a T2*-weighted anatomical reference dataset was also acquired using the same EPI pulse sequence, modified to provide whole-brain coverage but retaining the orientation and shimming volume of the partial-brain data (126 coronal slices, TR = 3.29 s). For both the functional runs and the anatomical reference scan, an additional volume was collected having opposite phase encoding, which was used to estimate and correct susceptibility-induced distortion (topup, FSL). Concurrent with MRI scanning, electrocardiogram (ECG) and respiration signals were continuously collected at 500 Hz using an MRI-compatible, noninvasive BIOPAC MP150 system (BIOPAC Systems, Goleta, CA, USA) and a laptop equipped with Acknowledge acquisition software (BIOPAC Systems).

MRI data preprocessing

For fMRI, data preprocessing was performed using a combination of the Oxford Centre for Functional MRI of the Brain (FMRIB) Software Library (FSL; v. 5.0.7), the Analysis of Functional Neuro-Images (AFNI), and in-house bash scripts. The fMRI images were corrected for cardiorespiratory noise (RETROICOR), slice timing (using a custom script accounting for the Simultaneous Multi-Slice acquisition of the dataset), susceptibility-induced distortion (estimated using topup, FSL), and head motion (MCFLIRT, FSL). Following these preprocessing steps, the whole-brain volume, sharing the same orientation and distortion as the partial-brain

fMRI runs, was normalized to a T2-weighted MNI template (ICBM 2009a Nonlinear Asymmetric template [36]) using linear and nonlinear transformations (FSL FLIRT and FNIRT, respectively). The high spatial resolution (1.2 mm isotropic voxels) and strong tissue contrast afforded by ultrahigh-field imaging allowed us to avoid the additional step of functional-to-anatomical co-registration, thus reducing possible misalignments due to variable susceptibility-induced distortion across sequences. A brainstem mask, defined in the ICBM152 MNI space by thresholding gray and white matter tissue maps at a tissue probability of 0.9 (as in prior studies [12,37,38]), was then transformed into individual functional spaces by inverting the estimated transform matrices (Fig. 2A). This mask was used to select and retain only brainstem fMRI voxels from the original dataset, in order to remove spatial smoothing-induced contamination of parenchymal voxels with fMRI signal from vascular and other non-parenchymal structures surrounding the brainstem such as cerebrospinal fluid (CSF), known to be heavily affected by physiological noise. Following this masking step, minimal spatial smoothing with a Gaussian smoothing kernel (full width at half maximum (FWHM) = 2 mm) was applied to the BOLD fMRI data.

MRI data analysis

For auricular stimulus fMRI scan runs, first-level General Linear Model (GLM) analyses of brainstem fMRI data were carried out using an event-related design and the fMRI Expert Analysis Tool (FEAT v6.00, FSL). Because the hemodynamic impulse response may deviate from the canonical hemodynamic impulse response function due to our target brainstem location, for each fMRI scan run, stimulation timings were convolved with a set of three basis functions chosen through FMRI's Linear Optimal Basis Set (FLOBS, FSL) algorithm, designed to provide flexibility in the shape of the hemodynamic response function. To account for the potential for the brainstem response to be faster than the canonical response [39], the FLOBS basis set was designed to span hemodynamic delays

between 1 and 8 s. Brainstem response to sham stimulation (exhalation-gated sham, eSham, and inhalation-gated sham, iSham) was assessed to control for any generalized fMRI signal response to neural or non-neural respiratory-based modulation. For both eSham and iSham, we used the respiratory signal collected during the corresponding fMRI scan run to define sham stimulus events for event-related fMRI analyses, thereby controlling for respiratory cycle influence on the brainstem fMRI signal. To further control for cardiac-driven contamination of the brainstem fMRI signal, instantaneous heart rate, as estimated through the point-process algorithm (see below), was convolved with the previously-reported cardiac response function [40] and included in the design matrix as a regressor of no interest.

Following this first level analysis, individual parameter estimates (PEs) derived from the three FLOBS basis functions were combined in a signed root mean square (RMS) summary statistic [41]. The resulting distribution of this summary statistic is highly non-Gaussian, therefore all group-level analyses were carried out using nonparametric permutation analysis (5000 randomizations; randomise, FSL). Individual summary statistics were then transformed to MNI space and concatenated for each condition, and brainstem responses were evaluated by comparing each active stimulation condition with the appropriate sham stimulation condition, using paired non-parametric randomization tests: eRAVANS–eSham, iRAVANS–iSham, GANctrl–eSham. Two sets of analyses were performed. The first set was aimed at evaluating ipsilateral dorsal medullary response (site of primary synapse for afference from the auricle, e.g. NTS, spinal trigeminal nucleus (SpV)). We used a small-volume approach in which a search volume was defined in the dorsal medulla ipsilateral to the stimulation site, which was defined by a caudal limit set by the fMRI data field-of-view, a rostral limit set by the pontomedullary junction, and a ventral limit set by the reticular formation (Fig. 2C). Given to the limited signal-to-noise ratio (SNR) typical for brainstem responses [33,37,42], significance within this small-volume search space was set at uncorrected $p < 0.05$. Additionally, in the Supplementary

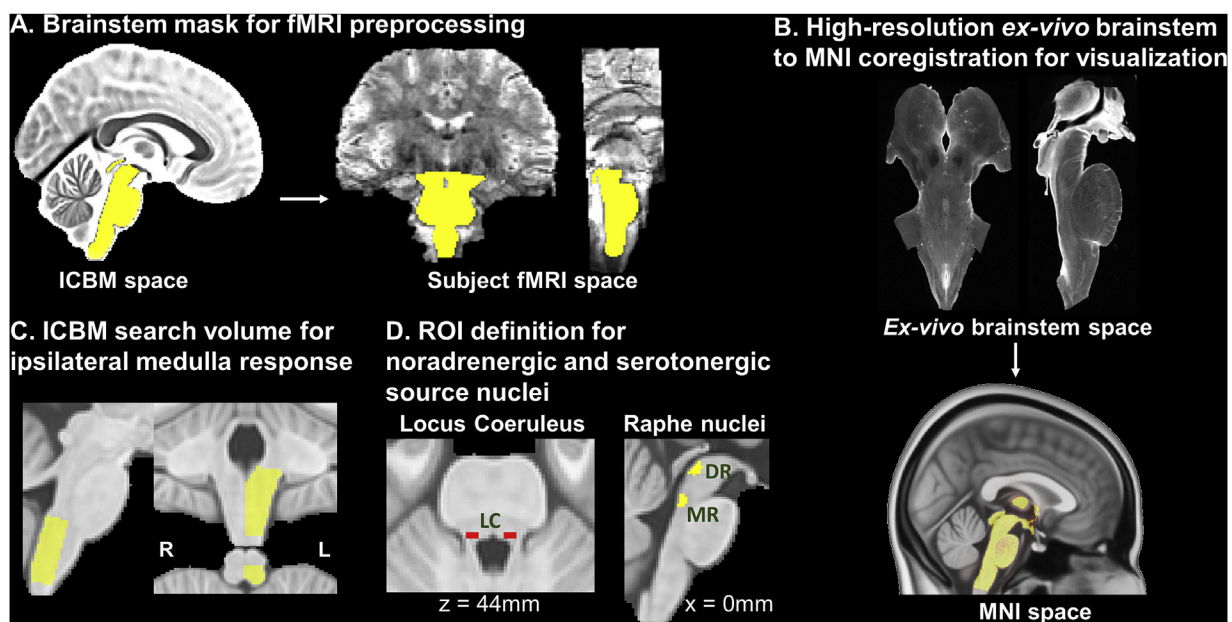


Fig. 2. (A) A brainstem mask defined in ICBM space was transformed to subjects' individual fMRI space and used to retain brainstem voxels and mitigate physiological noise contamination introduced by spatial smoothing. (B) A high-resolution (0.2 mm isotropic voxels) *ex vivo* brainstem volume (courtesy of [47]) was transformed to MNI space; transformation matrices were inverted and applied to the final group fMRI maps to aid visualization and comparison with brainstem atlases. (C) A volume including the left (ipsilateral to stimulation side) dorsal medulla was defined in ICBM space and used as a search space for evaluation of dorsal medullary brainstem responses to RAVANS and GANctrl stimulation runs. (D) ROIs for noradrenergic (LC; [45]) and serotonergic (DR, MR; [46]) nuclei were defined based on results of previous neuroimaging studies.

Material, we also display unmasked (whole-brainstem) results thresholded at uncorrected $p < 0.05$ (Supplementary Fig. S1). Significant fMRI clusters were localized with the aid of two brainstem atlases, Duvernoy's Atlas of the Human Brain Stem and Cerebellum [43] and Olszewski and Baxter's Cytoarchitecture of the Human Brainstem [44]. In a second analysis, the same contrasts were estimated in the entire brainstem volume, and a region of interest (ROI) approach was used with MNI-space masks for specific neurotransmitter nuclei hypothesized to be modulated by taVNS. These included bilateral locus coeruleus (LC), and dorsal and median raphe nuclei (DR, MR) (Fig. 2D), identified from results of previously published T1 turbo spin echo MRI [45] and [^{11}C]DASB positron emission tomography (PET) binding [46] neuroimaging studies specifically designed to identify these nuclei. For each ROI, an outcome metric was calculated with an Extent/Activation Index (EAI), defined as follows:

$$EAI_{ROI} = \frac{\text{sumstat}_{p < 0.05}}{\# ROI \text{ voxels}} \times \frac{\# \text{voxels}_{p < 0.05}}{\# ROI \text{ voxels}} \times 100$$

The EAI index weighs the average value of the FLOBS summary statistics from significant ($p < 0.05$) voxels within each ROI by a multiplicative factor quantifying the percentage of overlapping voxels with respect to the total number of voxels in the ROI, thus preventing a very significant, but spatially limited (i.e., a few voxels) activation from driving the outcome metric. The multiplicative factor is calculated at the group level for each condition (eRAVANS–eSham, iRAVANS–iSham, GANctrl–eSham), and then used to weigh the average value of the summary statistics over the ROI, extracted at the single subject level. The EAI indices for the different ROIs were then compared across conditions using paired t-tests. Significance was set at $p < 0.05$, Bonferroni-corrected for multiple comparisons.

Use of high-resolution anatomical underlay

In order to aid visualization and anatomical localization, functional activation results were displayed over an *ex vivo*, high resolution (0.2 mm isotropic) brainstem dataset (B_0 image from DTI acquisition) generously provided by the lab of Dr. Alan Johnson [47]. Accurate co-registration between this *ex vivo* brainstem volume and MNI space (which contained our fMRI maps) was performed using the Advanced Normalization Tools (ANTs) Toolbox [48] and 3D Slicer (www.slicer.org). Specifically, manual landmark-based affine registration was first completed using the first step of our previously published ABC brainstem co-registration method [49]. Subsequently, 3D Slicer was used to generate a brainstem mask on a 0.5 mm resolution MNI152 T1 template, which was dilated to include high-contrast boundaries and used to select the brainstem volume. The ANTs Toolbox was then used to perform a generic affine registration followed by Symmetric Normalization deformation using the default parameters and mutual information as similarity metric. Quality of co-registration was excellent for the medullary and pontine regions reported in our study (Fig. 2B, Supplementary Fig. S2). The estimated transformation matrices were then used to transform fMRI group level maps from MNI space to the high-resolution brainstem space for visualization.

Cardiovascular response analysis using instantaneous HF-HRV

For cardiovascular analysis, ECG segments relative to each run were first annotated to identify the R-wave peak using an automated in-house algorithm followed by manual inspection. Similar to our prior studies, a point-process method was used to develop local likelihood HR estimation from the R-to-R interval series [34].

Briefly, each series is modeled by an inverse Gaussian probability function describing the time interval before each successive heartbeat. The mean of this probability function is modeled using a linear autoregressive model of order k , thus characterizing the dependence of the current time interval on the last k beat-to-beat intervals. From this set of autoregressive coefficients, instantaneous spectral measures of heart rate variability (HRV) were integrated in canonical frequency bands, thus computing the power within the high-frequency (HF-HRV, 0.15–0.40 Hz) range [50]. As in our previous studies [51–53], the instantaneous HF-HRV index was chosen as a metric for parasympathetic (cardiovascular) activity, in order to estimate stimulus-evoked cardiovascular response. This instantaneous spectral approach allowed for assessment of peristimulus HF-HRV response to stimulation, not allowed by standard, non-time-varying frequency space HRV index estimation.

The instantaneous HF-HRV power time series were then segmented into individual epochs starting 0.5 s before each 1-s stimulation train, extending 2 s after the end of each stimulation (3.5 s epoch total duration). For analysis, pre-stimulation samples were used as a baseline, and percent HF-HRV variations were calculated for each event and averaged over the scan run and across subjects, in order to estimate the stimulus-evoked cardiovascular modulation response. Moreover, linear regression analysis evaluated any correlation between cardiovascular response and brainstem response for the ROIs defined above, using individual summary statistic values (significant at $p < 0.05$).

Results

All subjects tolerated the stimulation and completed the experimental sessions without adverse events. Stimulation characteristics across different conditions demonstrated no significant differences for stimulation current (F-score = 0.45, p -value = 0.64) or ratings of intensity (F-score = 0.06, p -value = 0.56) (Table 1). Individual current sensitivity across conditions was consistent – that is, subjects requiring higher stimulation currents in one stimulation run, also required higher currents in the others – as measured by a significant intraclass correlation coefficient (ICC = 0.75, p -value < 0.01). Trending, but non-significant differences, were noted for number of stimuli delivered (repeated measures ANOVA F-score = 2.58, p -value = 0.07) and inter-stimulus interval between stimuli (F-score = 2.67, p -value = 0.06), with slightly more stimuli and shorter ISI for iRAVANS on average. Furthermore, while order was randomized, no significant correlations were found between the order of active conditions (eRAVANS, iRAVANS, GANctrl) and stimulation characteristics or subjects' ratings.

Brainstem medullary response for each active condition was visualized over the high-resolution *ex vivo* dataset for localization (Fig. 3). Each active stimulation map was normalized by exhalation- or inhalation-gated sham stimulation fMRI response map, and the eRAVANS – eSham (hereinafter, eRAVANS') contrast showed a positive contrast (p -value < 0.05, uncorrected within the small-volume mask) in an elongated cluster extending rostro-ventrally within the rostromedial to rostralateral medulla. Based on

Table 1

Stimulation characteristics and subjects' ratings for the different conditions (mean \pm SD; ISI: inter-stimulus interval).

Condition	# stimuli	ISI (s)	Current (mA)	Intensity (0–10 NRS)
eSham/iSham	127.9 \pm 23.8	3.0 \pm 0.7	–	–
eRAVANS	127.5 \pm 22.0	2.9 \pm 0.6	1.6 \pm 2.3	4.5 \pm 0.8
iRAVANS	136.1 \pm 20.3	2.7 \pm 0.5	1.7 \pm 2.4	4.6 \pm 0.8
GANctrl	133.8 \pm 19.8	2.8 \pm 0.5	1.4 \pm 1.1	4.7 \pm 0.7

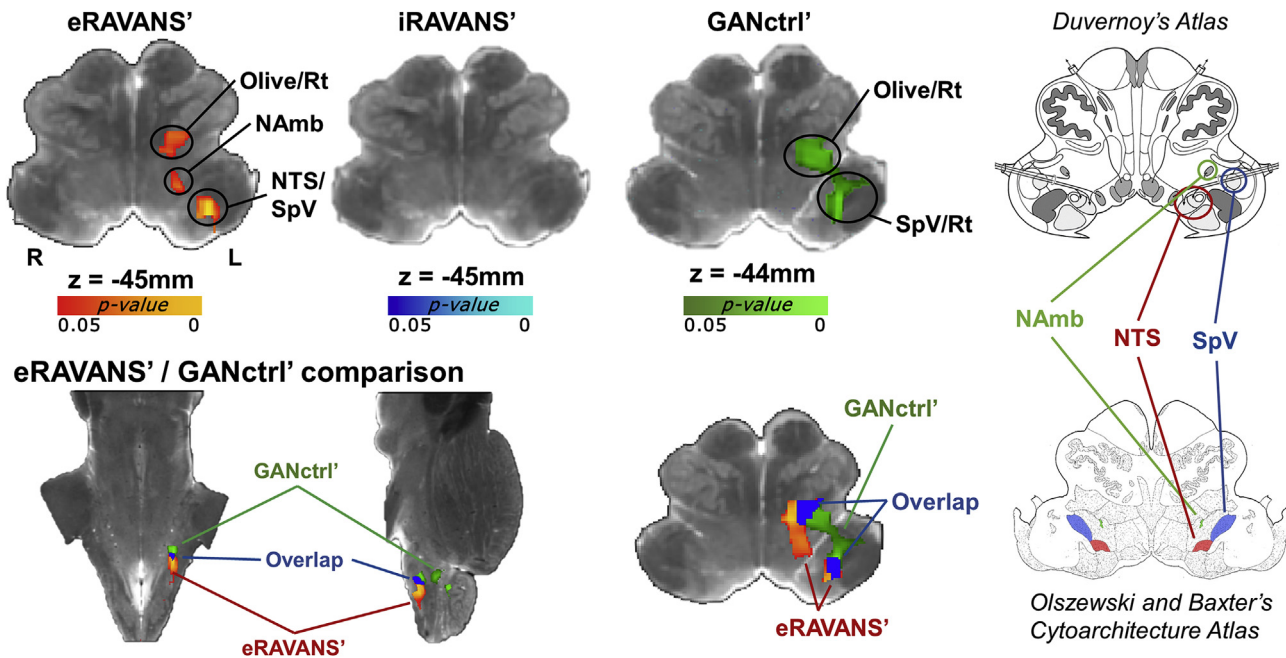


Fig. 3. Top row: group maps showing masked ipsilateral medullary responses to exhalatory taVNS (eRAVANS'), inhalatory taVNS (iRAVANS') and greater auricular nerve control stimulation over the earlobe (GANctrl'), overlaid on a high-resolution (0.2 mm) *ex vivo* brainstem. The respiration phase-matched sham (eSham, iSham) was subtracted from each active stimulation condition in order to normalize active stimulation response and control for respiratory modulation of the fMRI signal. Bottom row: eRAVANS' (red-yellow) and GANctrl' (green) group maps, as well as their overlap (blue), are shown on the same underlay. The corresponding brainstem slices from the Duvernoy's (top right) and the Olszewski and Baxter's (bottom right) atlases aid the localization of functional responses. The eRAVANS' cluster is consistent with purported NAmb, NTS and part of SpV, whereas the GANctrl' response mainly involves a cluster more consistent with SpV. (For interpretation of the references to colour in this figure legend, the reader is referred to the Web version of this article.)

brainstem atlases [43,44], this cluster encompassed purported rostral NTS, NAmb and the dorsoventral portion of the olivary nucleus. No significant responses were found for the iRAVANS – iSham (iRAVANS') contrast. While there were no significant differences found when directly contrasting eRAVANS and GANctrl, interesting offsets in localization were found for the normalized eRAVANS and GANctrl responses (red/yellow and green, respectively), as well as their overlap (blue) (Fig. 3). Results demonstrated that the GANctrl cluster had a more rostralateral location consistent with SpV, while the eRAVANS cluster was more dorsomedial and extended more caudally, consistent with the known anatomical morphology of NTS. When formally comparing eRAVANS and iRAVANS (i.e. eRAVANS' – iRAVANS', Fig. 4), a similar elongated cluster was revealed, and included rostral NTS and NAmb. The GANctrl – eSham (GANctrl') difference map showed a cluster located on the rostral edge of the search volume, and included purported dorsoventral olive/reticular formation, as well as SpV. The same analyses were repeated adding individual current levels as a regressor of no interest in the group design matrix, in order to control for the different current intensities due to our percept-matched approach to calibration. The resulting maps were nearly identical to those shown in Figs. 3 and 4, suggesting that current amplitude, while highly variable across subjects, did not significantly influence group differences.

In ROI analyses, significantly higher EAI values ($p < 0.05$, Bonferroni-corrected) were found for eRAVANS' compared to both iRAVANS' and GANctrl' in right LC (eRAVANS': 969.7 ± 1299.9 a. u., mean \pm SD; iRAVANS': 99.9 ± 302.9 a. u.; GANctrl': 114.8 ± 238.9 a. u.), DR nucleus (eRAVANS': 66.2 ± 100.8 a. u.; iRAVANS': 0 a. u.; GANctrl': 0 a. u.) and MR nucleus (eRAVANS': 867.7 ± 1184.9 a. u.; iRAVANS': 161.0 ± 402.6 a. u.; GANctrl': 0 a. u.) (Fig. 5).

Cardiovascular analysis found that compared to pre-stimulation baseline for each stimulus event, the HF-HRV stimulus-evoked

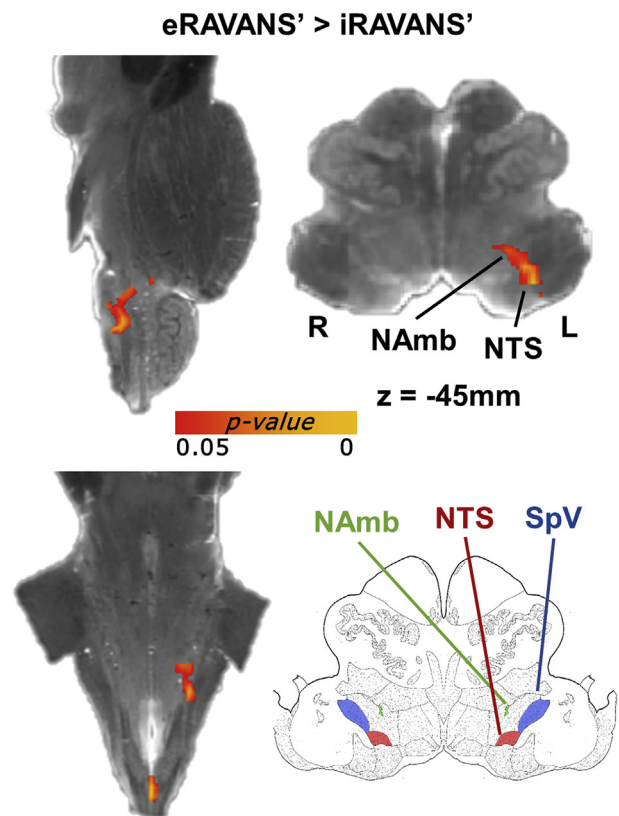


Fig. 4. Direct comparison between eRAVANS' and iRAVANS' responses noted greater NTS and NAmb activation for eRAVANS'.

ROI analysis – Extent Activation Index (EAI)

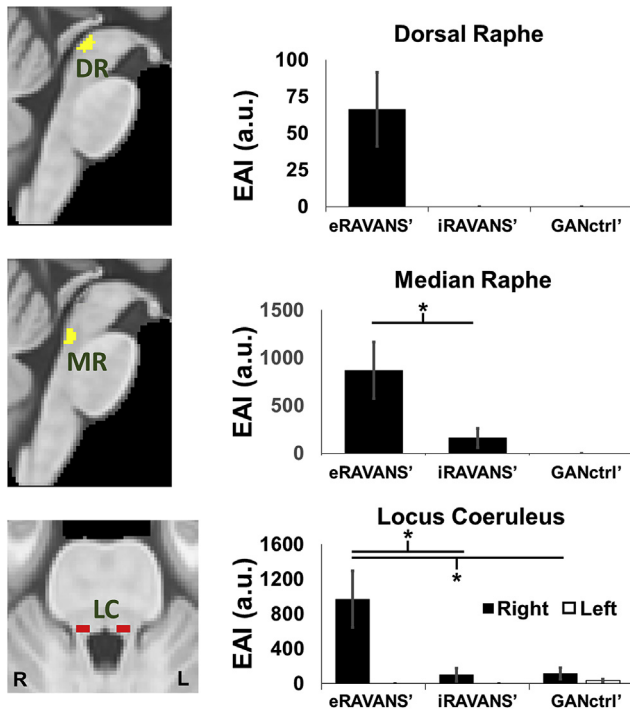


Fig. 5. ROI analysis found that eRAVANS' produced greater response than both iRAVANS' and GANctrl' in serotonergic (DR, MR) and noradrenergic (LC) source brainstem nuclei. Analyses use an Extent Activation Index (EAI), which weighted the activation strength by its extent within the ROI volume. * = $p < 0.05$; error bars show SEM.

response was significantly increased during the stimulation period for both eRAVANS' and GANctrl', while no significant deviation from baseline was found for iRAVANS' (Fig. 6A). Furthermore, cardiovagal response to eRAVANS showed increased values up to 2 s after the beginning of the stimulation period and the subjects' average HF-HRV change score in this 2 s post-eRAVANS onset window was correlated with fMRI response (FLOBS summary statistic) in the MR nucleus (Pearson's $r = 0.51$, p -value = 0.04; Fig. 6B). Thus, subjects with greater response in this serotonergic source nucleus also demonstrated greater cardiovagal modulation.

Discussion

The brainstem circuitry activated and modulated by taVNS has been challenging to evaluate in humans due to neuroimaging limits on spatiotemporal resolution and the strong physiological noise inherent to fMRI found within this important brain region [33]. Our study characterized brainstem response to taVNS applied to the cymba conchae of the left ear by exploiting the increased spatiotemporal resolution provided by ultrahigh-field (7T) fMRI. We explored the influence of respiratory phase on stimulation outcome by delivering stimulation during exhalation (eRAVANS) or inhalation (iRAVANS), and employed greater auricular nerve stimulation (GANctrl, electrodes placed on the earlobe) as a sensory control. Furthermore, we evaluated cardiovagal response (instantaneous HF-HRV) to stimulation, using cardiac data recorded concurrently with fMRI. For eRAVANS, we found stimulus-evoked activation in an ipsilateral pontomedullary region consistent with NTS, and activation was significantly more robust compared to inhalation-gated taVNS. Moreover, eRAVANS

activation in this region was partially overlapping but spatially offset from the ipsilateral pontomedullary region activated by GANctrl stimulation, which was consistent with the location of the SpV nucleus.

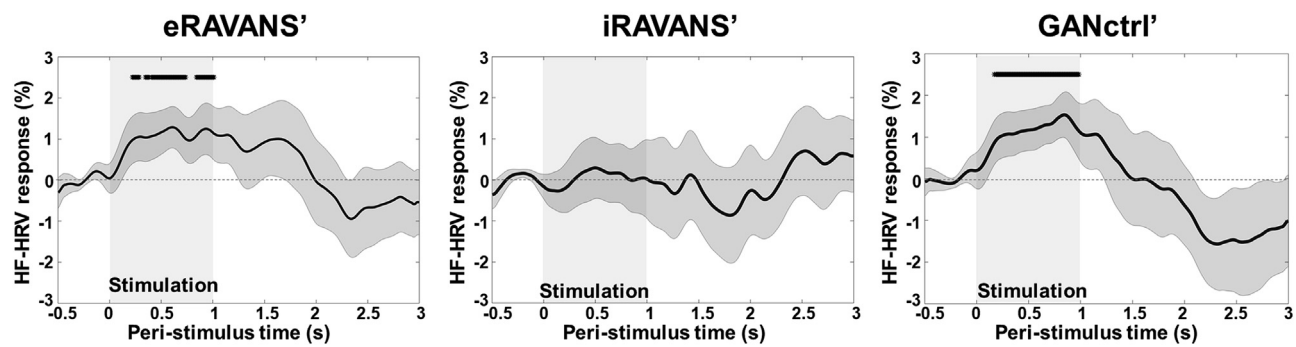
Additionally, an ROI analysis found greater activation for eRAVANS, compared to both iRAVANS and GANctrl, in important monoamine neurotransmitter source nuclei such as locus coeruleus (LC, noradrenergic) and median and dorsal raphe (MR, DR, serotonergic) nuclei. Furthermore, eRAVANS also increased HF-HRV, and greater increase in HF-HRV was associated with greater activation in the pontine median raphe nucleus. This suggests that this serotonergic source nucleus may play a role in the feedback regulatory loop by which auricular taVNS upregulates cardiovagal outflow. Our results localize taVNS targeting in the human brainstem, and demonstrate that exhalation-gated stimulation can enhance NTS targeting and cardiovagal modulation compared with inhalation-gated and sham control.

Results demonstrated enhanced ipsilateral NTS response for eRAVANS compared to iRAVANS. This nucleus is known to contain the primary synapse for ABVN afference into the brainstem, and a gateway by which ABVN stimulation can modulate higher brainstem and even cortical function in the brain. Thus, NTS activation could serve as a viable target for future taVNS optimization across different parameter spaces (e.g. frequency, pulse width, etc.). We proposed that a non-obvious parameter space includes respiratory phase, and attribute enhanced NTS activation during exhalation to both bottom-up and top-down influence. Firstly, the NTS receives afference during inhalation over the main trunk of the vagus from pulmonary stretch receptors and aortic baroreceptors [54], potentially competing with any ABVN afference to NTS. The NTS is also known to receive inhibitory inputs from ventral respiratory group (VRG) nuclei in the medulla during inhalation and facilitation during exhalation [23,24]. Ultimately, we suggest that both of these influences set up a more receptive state for ABVN input during exhalation.

We also found stimulus-evoked activation in other medullary nuclei, consistent with SpV and Namb, with greater activation for eRAVANS compared to iRAVANS. SpV is ventrolateral to NTS in the dorsal pontomedullary junction and is also known to receive afferent input over ABVN fibers [55,56]. Moreover, GANctrl stimulation also produced robust activation in ipsilateral medulla, in a cluster consistent with SpV, and ventrolateral to the NTS cluster activated by eRAVANS. The greater auricular nerve is a superficial cutaneous branch of the cervical plexus, composed of branches of spinal nerves C2 and C3, whose afferent fibers terminate in the cuneate and SpV nuclei in the medulla [57]. Thus, our GANctrl stimulation was not physiologically inert, and future studies evaluating clinical effects of taVNS should use caution in applying earlobe stimulation as a placebo control. In fact, its use has been recently debated in a series of commentaries [58,59], although no consensus has been reached regarding a suitable alternative.

On the other hand, Namb is a smaller-diameter elongated structure and the main premotor nucleus for vagal outflow to the heart. Respiratory phase may also be an important variable for stimulus-evoked response in this nucleus, as breathing is known to introduce rhythmical oscillations in cardiovagal physiology. During each respiratory cycle, heart rate decreases during exhalation and increases during inhalation, matching pulmonary blood flow to lung inflation and maintaining an appropriate oxygen diffusion gradient [60]. This "respiratory sinus arrhythmia" (RSA) occurs by modulation of premotor cardiovagal neurons (e.g. Namb) by diverse mechanisms, including afference (via NTS) from the lungs, and thoracic baroreceptors, as well as direct input from medullary respiratory neurons [60–62]. In fact, NTS neurons play a direct role in coordinating RSA [62], as activation of excitatory 2nd-order NTS

A. HF-HRV stimulus-evoked response



B. HF-HRV response is linked to median raphe (MR) response during eRAVANS

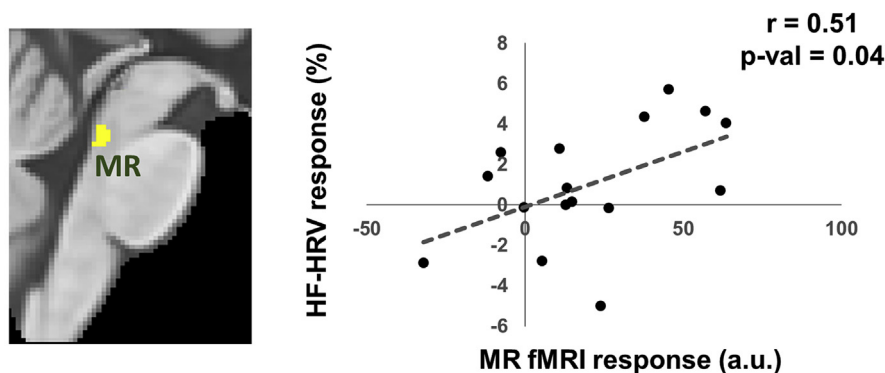


Fig. 6. (A) Stimulus-evoked HF-HRV power response to stimulation. eRAVANS' panel: * = eRAVANS > eSham, $p < 0.05$. GANctrl' panel: * = GANctrl > eSham, $p < 0.05$. (B) Subjects' stimulus-evoked HF-HRV response (0–2 s post-stimulation) was correlated with fMRI response in the MR nucleus (basis function summary statistic).

neurons increases premotor cardiovagal neuron firing rate and inhibits premotor sympathetic neurons [63,64]. In contrast, during inhalation, activity of ventral respiratory group medullary neurons leads to inhibitory GABAergic and glycinergic synaptic transmission to premotor cardiovagal neurons [65,66]. Our results show that ABVN input during exhalation also facilitates Namb activation.

Interestingly, eRAVANS evoked activation within important noradrenergic (LC) and serotonergic (MR, DR) brainstem source nuclei. Evoked fMRI response was significantly greater compared to both iRAVANS and GANctrl, suggesting that more robust NTS targeting also translates to greater activation of these higher pontine/midbrain nuclei. In fact, both noradrenergic and serotonergic regulation has been posited to be a mechanism supporting taVNS clinical outcomes [67]. LC, a columnar structure located bilaterally in the dorsal pons, contains the highest number of noradrenergic neurons in the brain, and is the origin of extensive and diffuse descending and ascending projections. The LC-noradrenaline system has been implicated in the modulation of a variety of higher cognitive and affective functions, including enhancement of arousal state [68,69], execution of adaptive behavioral responses [70], and memory consolidation and retrieval [71,72].

The raphe nuclei, on the other hand, are the largest collection of serotonergic neurons in the brain, and are clustered throughout the midline, extending from the medulla to the midbrain. The principal ascending fibers originate from MR and DR, located in the midbrain/pons and midbrain respectively, and target other midbrain nuclei, as well as subcortical and cortical structures [73,74]. Serotonin is a monoaminergic neuromodulator involved in a broad range of cognitive/affective functions including emotion

[75], reward [76], pain [77], sleep [78], and motor activity [79]. In sum, LC and raphe activation likely follows stimulation-evoked response in NTS, which is known from animal studies to project to peri-LC dendrites [21] and to midbrain raphe nuclei [80]. Furthermore, DR and MR nuclei receive substantial afferents from the parabrachial nucleus [81,82], which is also a target of NTS ascending fibers [22], and may modulate raphe nuclei activity by this indirect pathway.

Interestingly, our previous RAVANS fMRI study showed that following RAVANS there was increased LC and MR response to trigeminal sensory afference (forehead airpuff stimulation) in migraineurs [12], consistent with the hypothesis that serotonergic/noradrenergic regulation of abnormal trigeminal somatosensory processing supports the therapeutic effects of taVNS in migraine [14]. Our ultrahigh-field (7T) fMRI results demonstrated that eRAVANS also produces stimulus-evoked response in LC and raphe nuclei, more closely linking taVNS with serotonergic and noradrenergic regulation.

Additionally, cardiovagal modulation, as measured by instantaneous HF-HRV power, showed stimulus-evoked increase during eRAVANS and GANctrl stimulations, with more sustained response (up to 2 s after stimulation onset) for eRAVANS. No significant stimulus-evoked HF-HRV response was found for iRAVANS. These results are consistent with the brain imaging findings, confirming a lack of effect of iRAVANS at both central and peripheral neurophysiological levels. Interestingly, subjects with greater HF-HRV stimulus-evoked response for eRAVANS also demonstrated greater activation in MR. Midbrain raphe nuclei have been shown to modulate the activity of cell groups in the hypothalamus that are in

turn involved in autonomic control [83–86]. While this linkage between MR activation and HF-HRV power was found using group level analysis, a more direct linkage will likely require causality analyses on the individual level.

Our brainstem-focused fMRI analysis controlled for multiple factors known to reduce signal in brainstem fMRI data collection and analysis [33]. With regards to data collection, we positioned coronal slices along the longitudinal axis of the brainstem, thereby orienting our slices parallel to the long axis of most brainstem nuclei, including NTS, and parallel to the most prominent axis for cardiorespiratory-induced motion of the brainstem – i.e. cranio-caudal [87]. In terms of analysis approaches, we collected concurrent cardiac and respiratory data alongside the fMRI data to improve correction of physiological artifacts. Masking brainstem fMRI data prior to smoothing reduced the impact of cardiac pulsation noise from surface brainstem vessels and cerebrospinal fluid from spilling into parenchymal voxels of interest. Also, in computing subjects' evoked fMRI response maps, we used data from a no-stimulation sham control fMRI scan run for which an equivalent duration “event”-related regressor was created with equivalent timing during exhalation or inhalation. This allowed analyses to control for more general respiratory-linked fMRI signal fluctuation, thereby better isolating the true brainstem response to ABVN stimulation.

Another important point was that stimulation events were of short duration (1 s), thereby avoiding the known high noise regime that hamper fMRI designs using long stimulation blocks, as the power spectrum of BOLD fMRI noise decreases as $1/f$ with temporal frequency [88,89]. Previous taVNS fMRI studies have employed designs with long stimulus durations reflecting clinical parameters, and block lengths up to several minutes [26–29,31,32]. Such low task frequency designs might benefit from use of Arterial Spin Labeling fMRI techniques, which exhibit a flat power spectrum [90,91].

Our study also has limitations that should be discussed. For instance, BOLD fMRI signal responses in the brainstem have reduced SNR compared to cortical responses [33], leading to multiple brainstem fMRI studies using uncorrected thresholds, very low cluster-forming thresholds, or mask-based approaches to restrict the analysis to a smaller volume [28,29,31,32,92–94]. Nevertheless, the anatomical localization for NTS, Namb, and SpV in our study was consistent with the known targeting of ABVN and GAN nerve pathways into the medulla as noted by anatomical atlases and previously published results for specific trigeminal nuclei responding to orofacial nociceptive input [95–97]. These considerations increased our confidence that the reported activations do not constitute false positive results. Also, while a ROI approach for LC and raphe nuclei response constituted an unbiased framework for comparison, using anatomical ROIs has limitations, as only a subregion of LC and raphe nuclei could have been activated, leading to underestimated effect sizes.

In conclusion, our ultrahigh-field (7T) fMRI study demonstrated that exhalation-gated taVNS enhanced activation in ipsilateral NTS and up-stream monoaminergic source nuclei in the brainstem. eRAVANS also enhanced cardiovascular modulation. These results suggest recruitment of clinically-relevant neurophysiological pathways. Future studies need to explore longer-term physiological effects and explore additional parameters that may influence brain targeting for taVNS stimulation.

Conflicts of interest

VN discloses consulting fees from Glaxo Smith Kline and Cala Health, for whom he serves on the scientific advisory board; JG discloses consulting for Cala Health and serving on the scientific

advisory board. All other authors have no known conflicts of interest associated with this publication.

Acknowledgements

We thank the following organizations for funding support: US National Institutes for Health (NIH), Office Of The Director (OT2-OD023867); Center for Functional Neuroimaging Technologies (P41-EB015896); National Center for Complementary and Integrative Health, NIH (R61-AT009306, P01-AT006663, R01-AT007550); National Institute of Mental Health, NIH (R21-MH103468); National Institute of Arthritis and Musculoskeletal and Skin Diseases, NIH (R01-AR064367); the American Heart Association: (16GRNT26420084). This work also involved the use of instrumentation supported by the NIH Shared Instrumentation Grant Program and/or High-End Instrumentation Grant Program; specifically, Grant no. S1-ORR023043.

Appendix A. Supplementary data

Supplementary data to this article can be found online at <https://doi.org/10.1016/j.brs.2019.02.003>.

References

- [1] Ben-Menachem E, Manon-Espaillet R, Ristanovic R, Wilder B, Stefan H, Mirza W, Tarver W, Wernicke J. Vagus nerve stimulation for treatment of partial seizures: 1. A controlled study of effect on seizures. *Epilepsia* 1994;35(3):616–26.
- [2] Handforth A, DeGiorgio CM, Schachter SC, Uthman BM, Naritoku DK, Tecoma ES, Henry TR, Collins SD, Vaughn BV, Gilmartin RC, Labar DR, Morris 3rd GL, Salinsky MC, Osorio I, Ristanovic RK, Labiner DM, Jones JC, Murphy JV, Ney GC, Wheless JW. Vagus nerve stimulation therapy for partial-onset seizures: a randomized active-control trial. *Neurology* 1998;51(1):48–55.
- [3] Sackeim HA, Rush AJ, George MS, Marangell LB, Husain MM, Nahas Z, Johnson CR, Seidman S, Giller C, Haines S, Simpson Jr RK, Goodman RR. Vagus nerve stimulation (VNS) for treatment-resistant depression: efficacy, side effects, and predictors of outcome. *Neuropsychopharmacology* 2001;25(5):713–28.
- [4] Nemeroff CB, Mayberg HS, Kahl SE, McNamara J, Frazer A, Henry TR, George MS, Charney DS, Brannan SK. VNS therapy in treatment-resistant depression: clinical evidence and putative neurobiological mechanisms. *Neuropsychopharmacology* 2006;31(7):1345–55.
- [5] Ventureyra EC. Transcutaneous vagus nerve stimulation for partial onset seizure therapy. A new concept. *Child's Nerv Syst: ChNS: Official Journal of the International Society for Pediatric Neurosurgery* 2000;16(2):101–2.
- [6] Lehtimäki J, Hyvärinen P, Ylikoski M, Bergholm M, Makela JP, Aarnisalo A, Pirvola U, Makitie A, Ylikoski J. Transcutaneous vagus nerve stimulation in tinnitus: a pilot study. *Acta Otolaryngol* 2013;133(4):378–82.
- [7] Kreuzer PM, Landgrebe M, Resch M, Hüsner O, Schecklmann M, Geisreiter F, Poepl TB, Prasser SJ, Hajak G, Rupprecht R, Langguth B. Feasibility, safety and efficacy of transcutaneous vagus nerve stimulation in chronic tinnitus: an open pilot study. *Brain Stimul* 2014;7(5):740–7.
- [8] Rong P-J, Fang J-L, Wang L-P, Meng H, Liu J, Ma Y-g, Ben H, Li L, Liu R-P, Huang Z-X. Transcutaneous vagus nerve stimulation for the treatment of depression: a study protocol for a double blinded randomized clinical trial. *BMC Complement Altern Med* 2012;12(1):255.
- [9] Hein E, Nowak M, Kiess O, Biermann T, Bayerlein K, Kornhuber J, Kraus T. Auricular transcutaneous electrical nerve stimulation in depressed patients: a randomized controlled pilot study. *J Neural Transm* 2013;120(5):821–7 (Vienna, Austria: 1996).
- [10] Napadow V, Edwards RR, Cahalan CM, Mensing G, Greenbaum S, Valovska A, Li A, Kim J, Maeda Y, Park K, Wasan AD. Evoked pain analgesia in chronic pelvic pain patients using respiratory-gated auricular vagal afferent nerve stimulation. *Pain Medicine (Malden, Mass)* 2012;13(6):777–89.
- [11] Laqua R, Leutzow B, Wendt M, Usichenko T. Transcutaneous vagal nerve stimulation may elicit anti- and pro-nociceptive effects under experimentally-induced pain—a crossover placebo-controlled investigation. *Auton Neurosci* 2014;185:120–2.
- [12] Garcia RG, Lin RL, Lee J, Kim J, Barbieri R, Sclocco R, Wasan AD, Edwards RR, Rosen BR, Hadjikhani N, Napadow V. Modulation of brainstem activity and connectivity by respiratory-gated auricular vagal afferent nerve stimulation in migraine patients. *Pain* 2017;158(8):1461–72.
- [13] Janner H, Klausnitz C, Gurtler N, Hahnenkamp K, Usichenko TI. Effects of electrical transcutaneous vagus nerve stimulation on the perceived intensity

- of repetitive painful heat stimuli: a blinded placebo- and sham-controlled randomized crossover investigation. *Anesth Analg* 2018;126(6):2085–92.
- [14] Straube A, Ellrich J, Eren O, Blum B, Ruscheweyh R. Treatment of chronic migraine with transcutaneous stimulation of the auricular branch of the vagal nerve (auricular t-VNS): a randomized, monocentric clinical trial. *J Headache Pain* 2015;16:543.
 - [15] Clancy JA, Mary DA, Witte KK, Greenwood JP, Deuchars SA, Deuchars J. Non-invasive vagus nerve stimulation in healthy humans reduces sympathetic nerve activity. *Brain Stimulation* 2014;7(6):871–7.
 - [16] Antonino D, Teixeira AL, Maia-Lopes PM, Souza MC, Sabino-Carvalho JL, Murray AR, Deuchars J, Vianna LC. Non-invasive vagus nerve stimulation acutely improves spontaneous cardiac baroreflex sensitivity in healthy young men: a randomized placebo-controlled trial. *Brain Stimul* 2017;10(5):875–81.
 - [17] Badran BW, Mithoefer OJ, Summer CE, LaBate NT, Glusman CE, Badran AW, DeVries WH, Summers PM, Austelle CW, McTeague LM, Borckardt JJ, George MS. Short trains of transcutaneous auricular vagus nerve stimulation (taVNS) have parameter-specific effects on heart rate. *Brain Stimul* 2018b;11(4):699–708.
 - [18] Ylikoski J, Lehtimäki J, Pirvola U, Makitie A, Aarnisalo A, Hyvärinen P, Ylikoski M. Non-invasive vagus nerve stimulation reduces sympathetic preponderance in patients with tinnitus. *Acta Otolaryngol* 2017;137(4):426–31.
 - [19] Loewy AD, Burton H. Nuclei of the solitary tract: efferent projections to the lower brain stem and spinal cord of the cat. *J Comp Neurol* 1978;181(2):421–49.
 - [20] Norgren R. Projections from the nucleus of the solitary tract in the rat. *Neuroscience* 1978;3(2):207–18.
 - [21] Van Bockstaele EJ, Peoples J, Telegan P. Efferent projections of the nucleus of the solitary tract to peri-locus coeruleus dendrites in rat brain: evidence for a monosynaptic pathway. *J Comp Neurol* 1999;412(3):410–28.
 - [22] Saper CB, Stornetta RL. Central autonomic system. The rat nervous system. fourth ed. Elsevier; 2015. p. 629–73.
 - [23] Miyazaki M, Arata A, Tanaka I, Ezure K. Activity of rat pump neurons is modulated with central respiratory rhythm. *Neurosci Lett* 1998;249(1):61–4.
 - [24] Miyazaki M, Tanaka I, Ezure K. Excitatory and inhibitory synaptic inputs shape the discharge pattern of pump neurons of the nucleus tractus solitarii in the rat. *Exp Brain Res* 1999;129(2):191–200.
 - [25] Baek DM, Molkov YI, Paton JF, Rybak IA, Dick TE. Effect of baroreceptor stimulation on the respiratory pattern: insights into respiratory-sympathetic interactions. *Respir Physiol Neurobiol* 2010;174(1–2):135–45.
 - [26] Kraus T, Hösl K, Kiess O, Schanze A, Kornhuber J, Forster C. BOLD fMRI deactivation of limbic and temporal brain structures and mood enhancing effect by transcutaneous vagus nerve stimulation. *J Neural Transm* 2007;114(11):1485–93 (Vienna, Austria: 1996).
 - [27] Dietrich S, Smith J, Scherzinger C, Hofmann-Preiss K, Freitag T, Eisenkolb A, Ringler R. A novel transcutaneous vagus nerve stimulation leads to brainstem and cerebral activations measured by functional MRI. *Biomed Tech* 2008;53(3):104–11.
 - [28] Kraus T, Kiess O, Hösl K, Terekhin P, Kornhuber J, Forster C. CNS BOLD fMRI effects of sham-controlled transcutaneous electrical nerve stimulation in the left outer auditory canal – a pilot study. *Brain Stimul* 2013;6(5):798–804.
 - [29] Frangos E, Ellrich J, Komisaruk BR. Non-invasive access to the vagus nerve central projections via electrical stimulation of the external ear: fMRI evidence in humans. *Brain Stimulation* 2015;8(3):624–36.
 - [30] Usichenko T, Laqua R, Leutzow B, Lotze M. Preliminary findings of cerebral responses on transcutaneous vagal nerve stimulation on experimental heat pain. *Brain Imaging Behav* 2017;11(1):30–7.
 - [31] Yakunina N, Kim SS, Nam EC. Optimization of transcutaneous vagus nerve stimulation using functional MRI. *Neuromodulation* 2017;20(3):290–300.
 - [32] Badran BW, Dowdle LT, Mithoefer OJ, LaBate NT, Coatsworth J, Brown JC, DeVries WH, Austelle CW, McTeague LM, George MS. Neurophysiologic effects of transcutaneous auricular vagus nerve stimulation (taVNS) via electrical stimulation of the tragus: a concurrent taVNS/fMRI study and review. *Brain Stimul* 2018a;11(3):492–500.
 - [33] Sclocco R, Beissner F, Bianciardi M, Polimeni JR, Napadow V. Challenges and opportunities for brainstem neuroimaging with ultrahigh field MRI. *Neuroimage* 2018;168:412–26.
 - [34] Barbieri R, Matten EC, Alabi AA, Brown EN. A point-process model of human heartbeat intervals: new definitions of heart rate and heart rate variability. *Am J Physiol Heart Circ Physiol* 2005;288(1):H424–35.
 - [35] Polimeni JR, Bhat H, Witzel T, Benner T, Feiweier T, Inati SJ, Renvall V, Heberlein K, Wald LL. Reducing sensitivity losses due to respiration and motion in accelerated echo planar imaging by reordering the autocalibration data acquisition. *Magn Reson Med* 2016;75(2):665–79.
 - [36] Fonov V, Evans AC, Botteron K, Almli CR, McKinstry RC, Collins DL. Brain Development Cooperative G. Unbiased average age-appropriate atlases for pediatric studies. *Neuroimage* 2011;54(1):313–27.
 - [37] Beissner F, Baudrexel S. Investigating the human brainstem with structural and functional MRI. *Front Hum Neurosci* 2014;8:116.
 - [38] Moher Alsady T, Blessing EM, Beissner F. MICA—a toolbox for masked independent component analysis of fMRI data. *Hum Brain Mapp* 2016;37(10):3544–56.
 - [39] Lewis LD, Setsompop K, Rosen BR, Polimeni JR. Stimulus-dependent hemodynamic response timing across the human subcortical-cortical visual pathway identified through high spatiotemporal resolution 7T fMRI. *Neuroimage* 2018;181:279–91.
 - [40] Chang C, Cunningham JP, Glover GH. Influence of heart rate on the BOLD signal: the cardiac response function. *Neuroimage* 2009;44(3):857–69.
 - [41] Calhoun VD, Stevens MC, Pearlson GD, Kiehl KA. fMRI analysis with the general linear model: removal of latency-induced amplitude bias by incorporation of hemodynamic derivative terms. *Neuroimage* 2004;22(1):252–7.
 - [42] Brooks JC, Faull OK, Pattinson KT, Jenkinson M. Physiological noise in brainstem fMRI. *Front Hum Neurosci* 2013;7:623.
 - [43] Naidich TP, Duvernoy HM, Delman BN, Sorensen AG, Kollias SS, Haacke EM. Duvernoy's Atlas of the human brain Stem and Cerebellum. Vienna: Springer Vienna; 2009.
 - [44] Olszewski J, Baxter D. Cytoarchitecture of the human brain stem. In: Cytoarchitecture of the human brain stem; 1954.
 - [45] Keren NI, Lozar CT, Harris KC, Morgan PS, Eckert M. In vivo mapping of the human locus coeruleus. *Neuroimage* 2009;47(4):1261–7.
 - [46] Beliveau V, Svarer C, Frokjaer VG, Knudsen GM, Greve DN, Fisher PM. Functional connectivity of the dorsal and median raphe nuclei at rest. *Neuroimage* 2015;116:187–95.
 - [47] Calabrese E, Hickey P, Hulette C, Zhang J, Parente B, Lad SP, Johnson GA. Postmortem MRI of the human brainstem and thalamus for deep brain stimulator electrode localization. *Hum Brain Mapp* 2015;36(8):3167–78.
 - [48] Avants BB, Tustison NJ, Stauffer M, Song G, Wu B, Gee JC. The Insight Toolkit image registration framework. *Front Neuroinf* 2014;8:44.
 - [49] Napadow V, Dhond R, Kennedy D, Hui KK, Makris N. Automated brainstem co-registration (ABC) for MRI. *Neuroimage* 2006;32(3):1113–9.
 - [50] Camm AJMM, Malik M, Bigger JTGB, Breithardt G, Cerutti S, Cohen R, Coumel P, Fallen E, Kennedy H, Kleiger RE, Lombardi F. Heart rate variability: standards of measurement, physiological interpretation and clinical use. Task force of the European society of cardiology and the North American society of pacing and electrophysiology. *Circulation* 1996;93(5):1043–65.
 - [51] Napadow V, Dhond R, Conti G, Makris N, Brown EN, Barbieri R. Brain correlates of autonomic modulation: combining heart rate variability with fMRI. *Neuroimage* 2008;42(1):169–77.
 - [52] Sclocco R, Kim J, Garcia RG, Sheehan JD, Beissner F, Bianchi AM, Cerutti S, Kuo B, Barbieri R, Napadow V. Brain circuitry supporting multi-organ autonomic outflow in response to Nausea. *Cerebr Cortex* 2014;26:485–97 (New York, N.Y.: 1991).
 - [53] Sclocco R, Beissner F, Desbordes G, Polimeni JR, Wald LL, Kettner NW, Kim J, Garcia RG, Renvall V, Bianchi AM, Cerutti S, Napadow V, Barbieri R. Neuroimaging brainstem circuitry supporting cardiovagal response to pain: a combined heart rate variability/ultrahigh-field (7 T) functional magnetic resonance imaging study. *Philos Trans A Math Phys Eng Sci* 2016;374(2067).
 - [54] Piepoli M, Sleight P, Leuzzi S, Valle F, Spadacini G, Passino C, Johnston J, Bernardi L. Origin of respiratory sinus arrhythmia in conscious humans. An important role for arterial carotid baroreceptors. *Circulation* 1997;95(7):1813–21.
 - [55] Nomura S, Mizuno N. Central distribution of primary afferent fibers in the Arnold's nerve (the auricular branch of the vagus nerve): a transganglionic HRP study in the cat. *Brain Res* 1984;292(2):199–205.
 - [56] Kiyokawa J, Yamaguchi K, Okada R, Maehara T, Akita K. Origin, course and distribution of the nerves to the posterolateral wall of the external acoustic meatus. *Anat Sci Int* 2014;89(4):238–45.
 - [57] Liu D, Hu Y. The central projections of the great auricular nerve primary afferent fibers—an HRP transganglionic tracing method. *Brain Res* 1988;445(2):205–10.
 - [58] Keute M, Ruhnau P, Zaehle T. Reply to “reconsidering sham in transcutaneous vagus nerve stimulation studies. *Clin Neurophysiol* 2018;129(11):2503–4.
 - [59] Rangon CM. Reconsidering sham in transcutaneous vagus nerve stimulation studies. *Clin Neurophysiol* 2018;129(11):2501–2.
 - [60] Wehrwein EA, Joyner MJ. Regulation of blood pressure by the arterial baroreflex and autonomic nervous system. *Handb Clin Neurol* 2013;117:89–102.
 - [61] Dergacheva O, Griffioen KJ, Neff RA, Mendelowitz D. Respiratory modulation of premotor cardiac vagal neurons in the brainstem. *Respir Physiol Neurobiol* 2010;174(1–2):102–10.
 - [62] Zoccal DB, Furuya WI, Bassi M, Colombari DS, Colombari E. The nucleus of the solitary tract and the coordination of respiratory and sympathetic activities. *Front Physiol* 2014;5:238.
 - [63] Spyer KM. Neural organisation and control of the baroreceptor reflex. *Rev Physiol Biochem Pharmacol* 1981;88:24–124.
 - [64] Schreihofer AM, Guyenet PG. Baro-activated neurons with pulse-modulated activity in the rat caudal ventrolateral medulla express GAD67 mRNA. *J Neurophysiol* 2003;89(3):1265–77.
 - [65] Gilbey MP, Jordan D, Richter DW, Spyer KM. Synaptic mechanisms involved in the inspiratory modulation of vagal cardio-inhibitory neurones in the cat. *J Physiol* 1984;356:65–78.
 - [66] Neff RA, Wang J, Baxi S, Evans C, Mendelowitz D. Respiratory sinus arrhythmia: endogenous activation of nicotinic receptors mediates respiratory modulation of brainstem cardioinhibitory parasympathetic neurons. *Circ Res* 2003;93(6):565–72.
 - [67] Yuan H, Silberstein SD. Vagus nerve and vagus nerve stimulation, a comprehensive review: Part III. *Headache* 2015;56(3):479–90.
 - [68] Amatruda 3rd TT, Black DA, McKenna TM, McCarley RW, Hobson JA. Sleep cycle control and cholinergic mechanisms: differential effects of carbachol injections at pontine brain stem sites. *Brain Res* 1975;98(3):501–15.

- [69] Aston-Jones G, Bloom FE. Norepinephrine-containing locus coeruleus neurons in behaving rats exhibit pronounced responses to non-noxious environmental stimuli. *J Neurosci* 1981;1(8):887–900.
- [70] Aston-Jones G, Cohen JD. Adaptive gain and the role of the locus coeruleus-norepinephrine system in optimal performance. *J Comp Neurol* 2005;493(1):99–110.
- [71] Sara SJ. The locus coeruleus and noradrenergic modulation of cognition. *Nat Rev Neurosci* 2009;10(3):211–23.
- [72] Jacobs HI, Wiese S, van de Ven V, Gronenschild EH, Verhey FR, Matthews PM. Relevance of parahippocampal-locus coeruleus connectivity to memory in early dementia. *Neurobiol Aging* 2015;36(2):618–26.
- [73] Vertes RP, Linley SB. Efferent and afferent connections of the dorsal and median raphe nuclei in the rat. Serotonin and sleep: molecular, functional and clinical aspects. Springer; 2008. p. 69–102.
- [74] Dorocic IP, Fürth D, Xuan Y, Johansson Y, Pozzi L, Silberberg G, Carlén M, Meletis K. A whole-brain atlas of inputs to serotonergic neurons of the dorsal and median raphe nuclei. *Neuron* 2014;83(3):663–78.
- [75] Meneses A, Liy-Salmeron G. Serotonin and emotion, learning and memory. *Rev Neurosci* 2012;23(5–6):543–53.
- [76] Liu Z, Zhou J, Li Y, Hu F, Lu Y, Ma M, Feng Q, Zhang JE, Wang D, Zeng J, Bao J, Kim JY, Chen ZF, El Mestikawy S, Luo M. Dorsal raphe neurons signal reward through 5-HT and glutamate. *Neuron* 2014;81(6):1360–74.
- [77] Wang QP, Nakai Y. The dorsal raphe: an important nucleus in pain modulation. *Brain Res Bull* 1994;34(6):575–85.
- [78] Monti JM. The structure of the dorsal raphe nucleus and its relevance to the regulation of sleep and wakefulness. *Sleep Med Rev* 2010;14(5):307–17.
- [79] Di Matteo V, Pierucci M, Esposito E, Crescimanno G, Benigno A, Di Giovanni G. Serotonin modulation of the basal ganglia circuitry: therapeutic implication for Parkinson's disease and other motor disorders. *Prog Brain Res* 2008;172: 423–63.
- [80] Jacobs BL, Azmitia EC. Structure and function of the brain serotonin system. *Physiol Rev* 1992;72(1):165–229.
- [81] Saper CB, Loewy AD. Efferent connections of the parabrachial nucleus in the rat. *Brain Res* 1980;197(2):291–317.
- [82] Lee HS, Kim M-A, Valentino RJ, Waterhouse BD. Glutamatergic afferent projections to the dorsal raphe nucleus of the rat. *Brain Res* 2003;963(1):57–71.
- [83] Benarroch EE, Balda MS, Finkielman S, Nahmod VE. Neurogenic hypertension after depletion of norepinephrine in anterior hypothalamus induced by 6-hydroxydopamine administration into the ventral pons: role of serotonin. *Neuropharmacology* 1983;22(1):29–34.
- [84] Robinson SE, Austin MJ, Gibbens DM. The role of serotonergic neurons in dorsal raphe, median raphe and anterior hypothalamic pressor mechanisms. *Neuropharmacology* 1985;24(1):51–8.
- [85] Petrov T, Krukoff TL, Jhamandas JH. The hypothalamic paraventricular and lateral parabrachial nuclei receive collaterals from raphe nucleus neurons: a combined double retrograde and immunocytochemical study. *J Comp Neurol* 1992;318(1):18–26.
- [86] Bell AA, Butz BL, Alper RH. Cardiovascular responses produced by microinjection of serotonin-receptor agonists into the paraventricular nucleus in conscious rats. *J Cardiovasc Pharmacol* 1999;33(2):175–80.
- [87] Terem I, Ni WW, Goubran M, Rahimi MS, Zaharchuk G, Yeom KW, Moseley ME, Kurt M, Holdsworth SJ. Revealing sub-voxel motions of brain tissue using phase-based amplified MRI (aMRI). *Magn Reson Med* 2018;1:11.
- [88] Zarahn E, Aguirre GK, D'Esposito M. Empirical analyses of BOLD fMRI statistics. I. Spatially unsmoothed data collected under null-hypothesis conditions. *Neuroimage* 1997;5(3):179–97.
- [89] Birn RM, Cox RW, Bandettini PA. Experimental designs and processing strategies for fMRI studies involving overt verbal responses. *Neuroimage* 2004;23(3):1046–58.
- [90] Aguirre GK, Detre JA, Wang J. Perfusion fMRI for functional neuroimaging. *Int Rev Neurobiol* 2005;66:213–36.
- [91] Wang DJ, Chen Y, Fernandez-Seara MA, Detre JA. Potentials and challenges for arterial spin labeling in pharmacological magnetic resonance imaging. *J Pharmacol Exp Therapeut* 2011;337(2):359–66.
- [92] Hahn A, Kranz GS, Seidel E-M, Sladky R, Kraus C, Küblböck M, Pfabigan DM, Hummer A, Grahl A, Ganger S. Comparing neural response to painful electrical stimulation with functional MRI at 3 and 7 T. *Neuroimage* 2013;82:336–43.
- [93] Faull OK, Jenkinson M, Ezra M, Pattinson K. Conditioned respiratory threat in the subdivisions of the human periaqueductal gray. *Elife* 2016;5.
- [94] Frangos E, Komisaruk BR. Access to vagal projections via cutaneous electrical stimulation of the neck: fMRI evidence in healthy humans. *Brain Stimul* 2017;10(1):19–27.
- [95] Nash PG, Macefield VG, Klineberg JJ, Murray GM, Henderson LA. Differential activation of the human trigeminal nuclear complex by noxious and non-noxious orofacial stimulation. *Hum Brain Mapp* 2009;30(11):3772–82.
- [96] Nash PG, Macefield VG, Klineberg JJ, Gustin SM, Murray GM, Henderson LA. Bilateral activation of the trigeminothalamic tract by acute orofacial cutaneous and muscle pain in humans. *Pain* 2010;151(2):384–93.
- [97] Youssef AM, Gustin SM, Nash PG, Reeves JM, Petersen ET, Peck CC, Murray GM, Henderson LA. Differential brain activity in subjects with painful trigeminal neuropathy and painful temporomandibular disorder. *Pain* 2014;155(3):467–75.